Andrii CHEILYTKO, Oguzhan NOHUTCU
Peter SCHWARZBÖZL, Robin Tim BROESKE
German Aerospace Center (DLR), Institute of Solar Research, Karl-Heinz-Beckurts-Straße 6, 52428 Juelich, Germany
Corresponding author: andrii.cheilytko@dlr.de

Doi: 10.53412/jntes-2023-3-2

CFD SIMULATION OF AIRFLOW IN A NEW RECEIVER CONCEPT FOR SOLAR TOWER

Abstract: *Open cavity solar receivers play an important role in concentrated solar power (CSP) systems and hold great promise, particularly in scenarios where their ability to absorb high fluxes at very high temperatures yields beneficial results. This intense concentration of sunlight can be used to produce electricity through various means, such as generating steam to drive a turbine. The efficiency of the open volumetric receiver concept relies heavily on the air return ratio (ARR) which refers to the proportion of air recirculated and returned to the receiver. A high ARR contributes to high receiver efficiencies, as with rising ARR, the reused part of the enthalpy of warm air increases. This paper deals with the design and simulation of a new receiver concept with a conical cavity and square cross-section. The objective is to identify the most effective design arrangement for the square-cone structure, considering different depths, that maximizes both the air return ratio (ARR) and thermal efficiency. The findings demonstrate that increasing the depth of the mentioned receiver leads to a rise in the ARR, up to a certain threshold which can reach values up to 94.53%, beyond which there is a subsequent decline in efficiency. Furthermore, this study examined how varying the amount of air passing through a specific section of the receiver across a defined area, along with the temperature changes in these sections, affected its operational efficiency.*

Keywords: *solar tower, cavity receiver, air return ratio, convective efficiency, CFD simulation, airflow analysis.*

Introduction

CSP offers the benefit of storing generated energy and providing a continuous supply when needed. Its high energy efficiency makes it a competitive alternative to coal and nuclear power plants [1]. These aspects make this technology an attractive option for meeting future energy needs. One type of CSP is solar towers, which use different kinds of solar receivers to convert solar radiation into thermal energy.

Open volumetric receiver (OVR) technology stands out as an interesting advancement in concentrated solar power (CSP) because of the high temperatures that can be reached by the heat transfer fluid (air at ambient pressure), leading to a highly efficient power cycle. The design of OVRs allows the receiver to interact with the surrounding atmosphere and adjust the amount of air accordingly. Depending on the particular application and limitations, their shapes and arrangements may differ, commonly taking on cylindrical or rectangular forms with suitable openings or connections for air intake and outlet [2].

Figure 1 depicts the basic layout of the cavity receiver, which has a modular receiver concept. Each receiver module was constructed as an open cavity with an inner square cone shape. In the illustrated model, air entered the cavity through the inlet absorber, which was first heated to 450°C. Once inside the cavity, air is sucked through the main absorber, where it reaches its eventual temperature of 700°C.

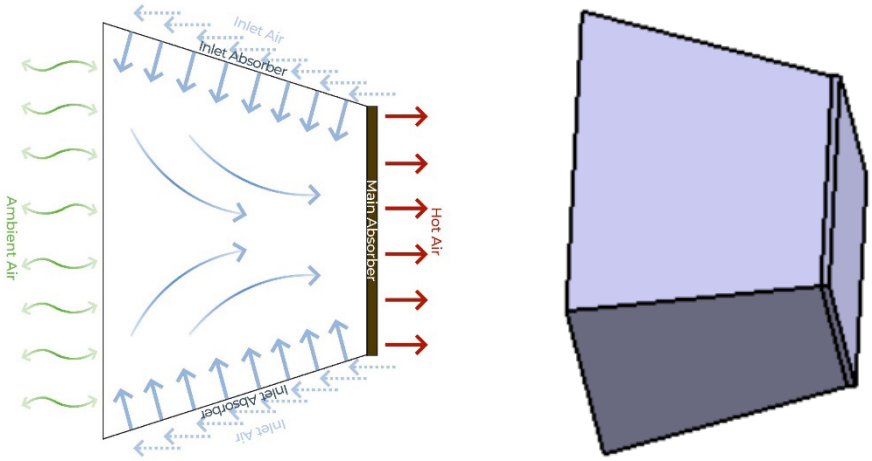

Figure 1. *Illustration of the new concept of cavity receiver for solar tower*

To understand the ARR of a cavity receiver, it is important to point out this parameter. The ARR represents the fraction of the inlet air redirected back into the main absorber (Equation 1).

$$\mathrm{ARR} = \frac{\dot{m}_{\mathrm{ReturnedInletAir}}}{\dot{m}_{\mathrm{HotAir}}} \tag{1}$$

A high ARR contributes to high receiver efficiencies because with rising ARR values, the reused part of the enthalpy of warm air increases. The ARR is of vital importance in maximizing receiver efficiency, especially when high return air temperatures are advantageous for subsequent processes [3].

Calculations of the air return ratio were conducted using ANSYS (Version 2023 R1). The ARR computations were conducted for four distinct setups, ranging from 50 mm to 200 mm, with intervals of 50 mm. The results demonstrate that the optimum ARR was achieved with an aperture depth of 150 mm.

Method and Model

For simplicity of explanation, the upcoming analyses will focus on the inner section of the cavity receiver. The computational fluid dynamics (CFD) software ANSYS CFX (Version 2023 R1) was employed to perform computations to determine the best variation for receiver configurations with varying aperture depths.

For the first part of the analysis, simulations were performed to determine the ARR, ultimately revealing which aperture depth provides the highest level of efficiency. In the depicted model, air at 450°C enters the cavity through the inlet absorber at a mass flow rate of 0.07 kg/s. Inside the cavity, the air undergoes a heating process until it reaches an eventual temperature of approximately 700°C.

In the second part of the model analysis both mass flow and temperature gradients will be introduced to the inlet of the receiver to investigate the influence of this parameters on the ARR.

Geometry. To determine the ideal design of the absorber, both simulation approaches were examined under different depth variations from 50 mm to 200 mm at intervals of 50 mm. All absorber designs have an aperture length of 200 mm, whereas the length of the top side was defined as 140 mm. The main absorber is a wire mesh absorber with a 5 mm thickness and has a porous structure, as shown in Figure 2. The main absorber in the designed model utilizes a volume porosity of 0.5.

The porosity of a material is a measure of its void space. The higher the porosity, the greater the void space in the material. As for the described model a porosity factor of 0.5 was applied. A porous surface enhances heat transfer and reduces thermal losses by increasing the surface area available for absorbing and transferring heat from the incoming air or heat transfer medium [4].

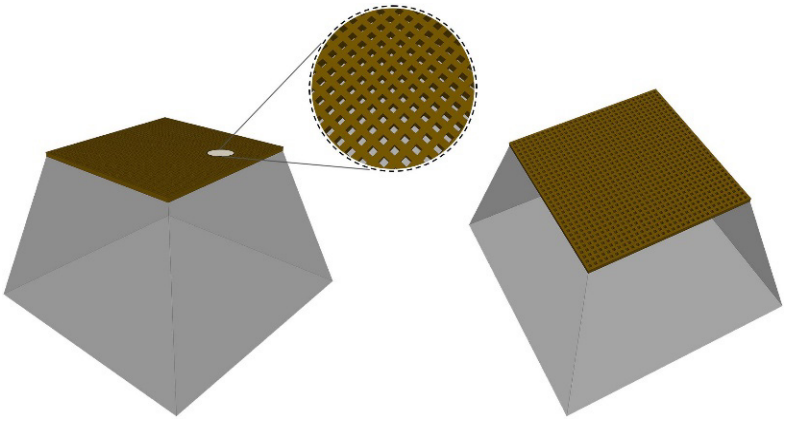

Figure 2. *Porous main absorber in new concept of receiver for solar tower (wire mesh region for inlet absorber not shown)*

Mesh Method. The examination of the square-cone shaped receiver covers two distinct points: determination of the optimal design for the receiver and subsequently analysis of the effect of both a mass flow gradient and temperature gradient to assess their respective influences on the ARR.

The computational grids employed for the model are composed of structured meshes, generated using ANSYS. Structured meshes comprise orderly grids featuring a consistent layout, making them suitable for relatively uncomplicated and uniform shapes. When dealing with geometries that align effectively with these grids, this mesh type can result in a more accurate portrayal of flow and heat transfer phenomena [5].

To determine the optimal geometry, a methodology referred to as "approach one" was employed. To represent the airflow between the opening of the receiver and surrounding a computational space for the ambient was added to the model. The computational space for the ambient has a domain length of five times the receiver's dimension along the direction of the flow, with a width twice that of the receiver to provide enough space for the flow to adjust to the presence of the geometry as suggested by Cagnoli et al. [6].

As evident in the Figure 3, the mesh becomes more refined towards the edges of the receiver. This refinement enhances the resolution, enabling a more detailed analysis of buoyancy effects and boundary conditions.

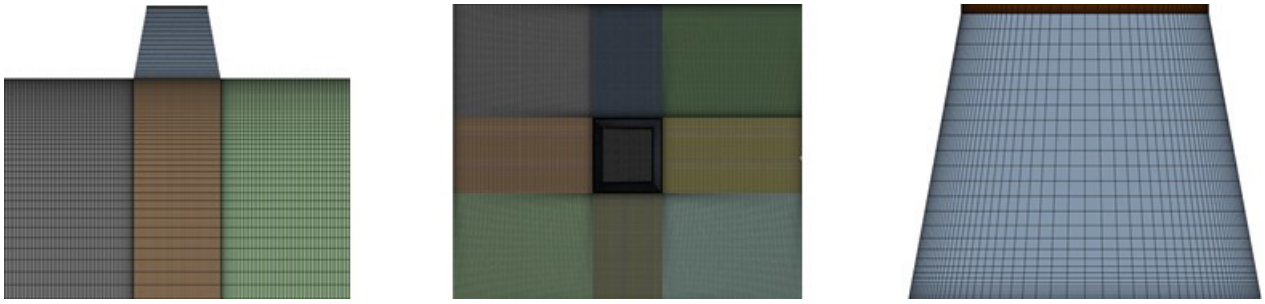

(a) Front View (b) Top View (c) Receiver

Figure 3. *Meshing for approach one*

For the second approach, shown in Figure 4, the absorber configuration is divided into five distinct segments. This segmentation allows for the integration of varying mass flow and temperature gradients, ultimately contributing to the calculation of their respective ARR values at a later stage. To further enhance the precision of the outcomes, the mesh was configured to be more refined at the interfaces between these sections and denser towards the edges. This approach mirrors the technique previously employed in approach one, ensuring a thorough and accurate analysis.

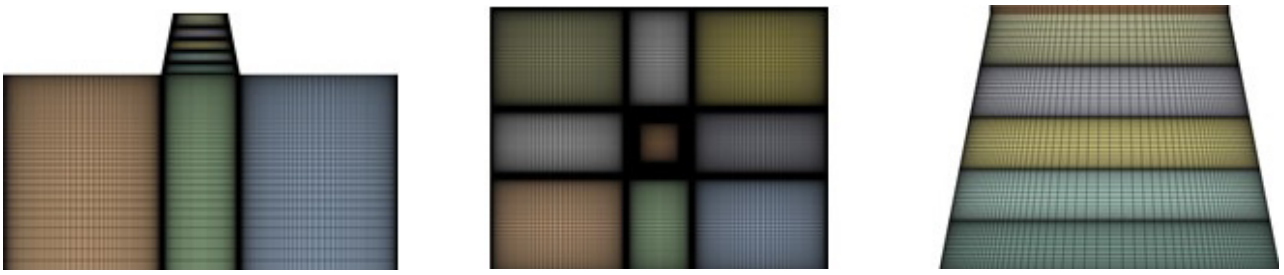

(a) Front View (b) Top View (c) Receiver

Figure 4. *Meshing for approach two*

Simulation Strategy. Having a good configuration for the simulation setup of the CFD model is an essential task, and particular attention is paid to these conditions due to their critical role in achieving precise solutions for fluid flow and heat transfer calculations.

The examination will employ the pressure-based methodology, as it deals with low-speed, incompressible airflow for the receiver. The model incorporates two distinct phases of air, each treated as an ideal gas, one for the incoming air and another for the ambient, indicating the utilization of multiphase simulations.

It is important to select a reasonable turbulence model that aligns with the constructed model. Given these considerations, the *k*-omega-SST turbulence model emerges as the most appropriate choice. This model aligns well with the structured meshes employed for the receiver, particularly in scenarios when dealing with complex flows [7].

Theory and Calculation

Efficiency calculations were conducted to assess the effectiveness of the receiver variations. An efficiency of 1, or 100%, if expressed as a percentage, indicates a perfectly efficient system in which all inputs are converted into useful outputs. In real-world scenarios, this is rarely achieved, owing to the manifold losses experienced by the receiver. In the context of this paper the convective efficiencies of the respective receivers will be derived.

Various approaches can be used to compute the convective efficiency of the system. Here, the efficiency ratios are calculated using the return efficiency methodology outlined by Cheilytko A. et al. [8]:

$$Q_{\text{full}} = Q_{\text{useful}} + Q_{\text{loss}} \tag{2}$$

$$1 = \eta_{conv} + \frac{Q_{\text{loss}}}{Q_{\text{full}}} \tag{3}$$

$$\eta_{conv} = 1 - q_{\text{loss}}^{\text{air}} \tag{4}$$

Equation (2) to Equation (4) outlines the derivation of the return efficiency method, where the convective heat loss is subtracted from 1. This resultant value is then interpreted as the convective heat efficiency of the receiver. Equation (5) can be used to compute $q_{\text{loss}}^{\text{air}}$ once the necessary values $Q_{\text{loss}}^{\text{air}}$ and I_{rec} are acquired for the system:

$$q_{\text{loss}}^{\text{air}} = \frac{Q_{\text{loss}}^{\text{air}}}{I_{\text{rec}}} \tag{5}$$

$Q_{\text{loss}}^{\text{air}}$ represents the energy loss owing to the heat from the air leaving the solar plant to the environment. To derive $Q_{\text{loss}}^{\text{air}}$ (Eq. 6) for the calculation of $q_{\text{loss}}^{\text{air}}$ the obtained ARR values (Table 1) for varying receiver depths were used. Additionally, the enthalpy values for the ambient and inlet air are obtained from the heat atlas [9]. The enthalpy values are primarily dependent on the temperature of the

air as an ideal gas, which is 22°C for the ambient temperature and 450°C for the inlet. At these respective states the enthalpies are respectively -3.01 kJ/kg and 440.330 kJ/kg. ε is a delay factor related to the time required to heat the exhaust air to a given temperature, which will be taken 1 for the upcoming calculations since we are dealing with stationary case [10].

$$Q_{loss}^{air} = \left(H_{out}^{air} - H_{amb}^{air}\right) \cdot \left(1 - ARR\right) \cdot \varepsilon \tag{6}$$

where:

H_{out}^{air} – enthalpy carried by air (kJ/s);

H_{amb}^{air} – enthalpy brought in with ambient air (kJ/s);

ε – delay factor.

I_{rec} is the power received from sunlight on the surface of the receiver, determined by both the aperture area of the receiver and the incident solar radiation. The previously computed incoming solar radiation directed at the receiver was established in Solar Tower Juelich (STJ).

In ANSYS CFX environment, the corresponding ARR values were calculated for different receiver depths, as listed in the table below.

Table 1. *ARR values obtained for different geometry variations*

h **[mm]**	***ARR*** **[%]**
50	87.66
100	92.90
150	94.53
200	94.24

Upon calculating the total loss by integrating the derived values into the respective equations, the corresponding convective efficiency values for the geometric alterations are listed below.

Table 2. *Convective heat efficiency distribution for different geometry variations*

h **[mm]**	***η*** **[%]**
50	88.03
100	93.11
150	94.69
200	93.44

Comparing these two tables, it can be concluded that the convective heat efficiency is proportional to ARR.

Results

Analysis on the Receiver Geometry. The assessments provided in this section rely on CFD simulations conducted using ANSYS CFX. The data under examination were obtained from steady-state RANS calculations. Post-processing of the effects and results was conducted and analyzed using the CFX post. These effects are visualized in the model developed by contour plots and gradients of various flow quantities contained in the output dataset. This allowed for the visualization and examination of the air entering the receiver and exiting the main absorber. The optimal variation is emphasized by evaluating diverse geometric alterations. This will allow conclusions to be drawn about the effects of geometry adaptations and the consequences of the mass flow and temperature gradients.

Thermal Analysis. The thermal efficiency analysis was performed by analyzing the contour plots shown in Figure 5. Because the receiver contains an aperture, a portion of the exhausted air is naturally lost to the ambient air and substituted with the surrounding air as a consequence of the buoyancy effect.

Buoyancy effects can have a significant impact on the efficiency of cavity-air receivers. Contour plots of the total inlet air temperature were used to analyze these effects. During the heating process, the receiver becomes less dense and rises owing to the buoyancy. This creates a natural flow circulation resulting from the cooler air entering the bottom and warmer air rising to the top [11]. This circulation helps to distribute heat more evenly within the receiver, which can improve the overall efficiency. It is evident from Figure 5 that the best heat distribution was achieved at a depth of 150 mm. The heat was almost evenly distributed over the walls of the receiver, contributing to the maintenance of a more stable and efficient operation. For other variations, some localized overheating can be observed, which can lead to potential structural damage. By maintaining more uniform temperatures, buoyant flow can help reduce thermal stress on the receiver material, which can lead to a longer lifespan of the receiver and improve its overall reliability.

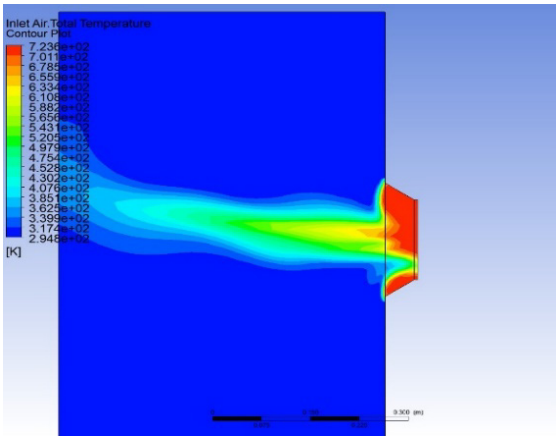

(a) Inlet total temperature contour for 50 mm depth

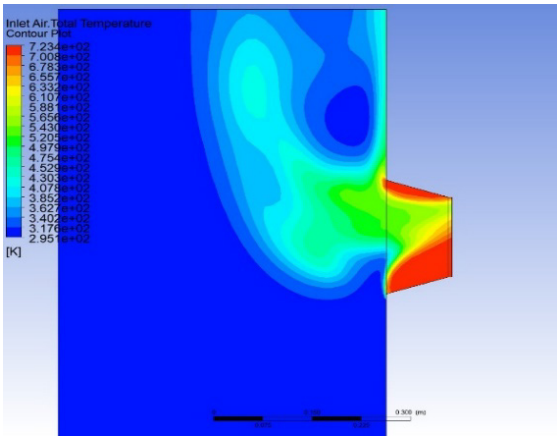

(b) Inlet total temperature contour for 100 mm depth

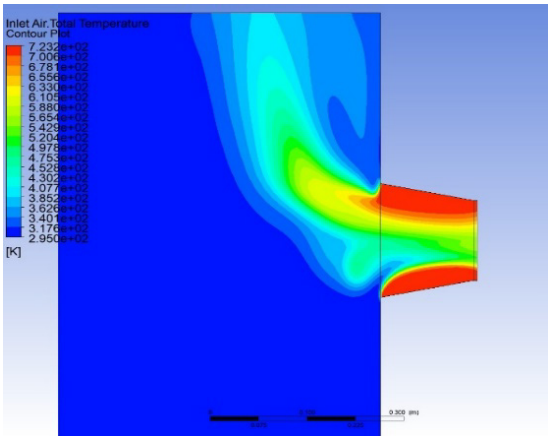

(c) Inlet total temperature contour for 150 mm depth

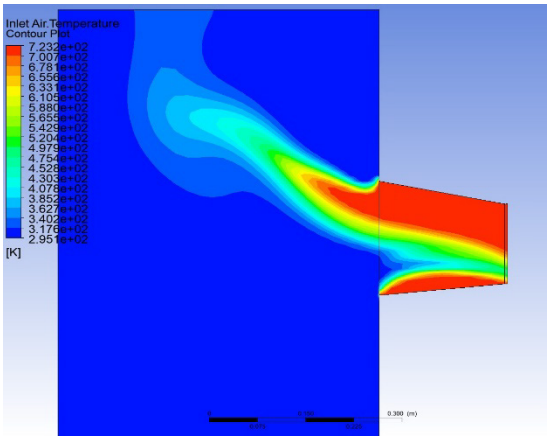

(d) Inlet total temperature contour for 200 mm depth

Figure 5. *Comparison of the inlet total temperature contour plots for the different geometry variations*

Analysis of the Effect of the Receiver Depth on the ARR. An examination will be conducted focusing on the ARR with respect to receiver depths of different variations. The analysis was facilitated by the generation of contour plots representing the inlet air velocity. This visualization technique offers a deeper understanding of how varying receiver depths affect ARR. The figures above show the partial loss of warm air from the environment. As losses increase, ARR decreases, and thus, efficiency decreases.

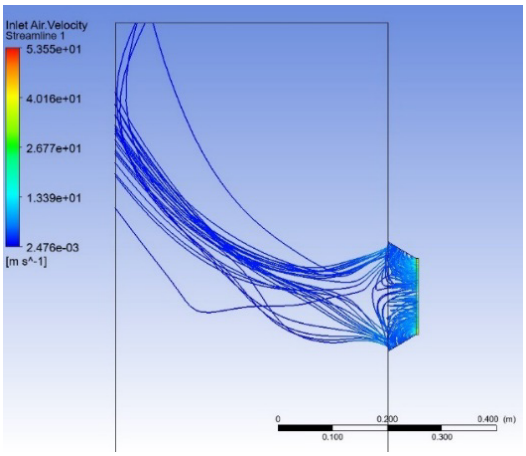

(a) Partial loss of warm air to the ambient for 50 mm depth

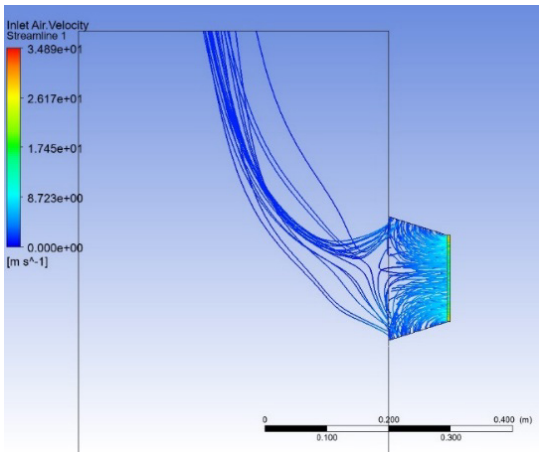

(b) Partial loss of warm air to the ambient for 100 mm depth

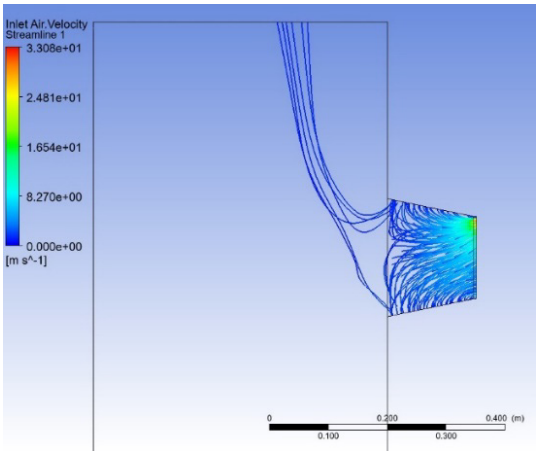

(c) Partial loss of warm air to the ambient for 150 mm depth

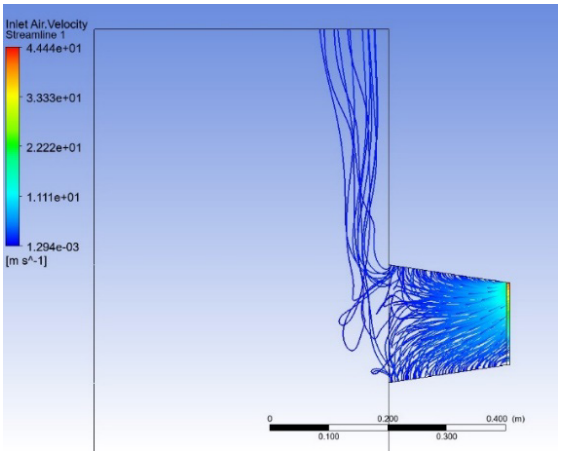

(d) Partial loss of warm air to the ambient for 200 mm depth

Figure 6. *Comparison of the partial loss of warm air to the ambient for different geometry variations*

An examination will be conducted focusing on the ARR with respect to receiver depths of different variations. The analysis was facilitated by the generation of contour plots representing the inlet air velocity. This visualization technique offers a deeper understanding of how varying receiver depths affect ARR. The figures above show the partial loss of warm air from the environment. As losses increase, ARR decreases, and thus, efficiency decreases.

It should be noted that the heat dissipation to the ambient decreases steadily up to a receiver depth increase of 150 mm, but then starts to increase again. These contour plots validate the accuracy of the earlier calculations for the ARR. This indicates a critical point at a depth of 150 mm, beyond which the heat loss begins to increase.

Moreover, the flow dynamics within the receiver play a major role. As air flows into the receiver, it encounters resistance that is directly proportional to velocity leading to a pressure drop. The pressure subsequently leads to a decrease in the overall efficiency. As the velocity increases, the pressure drop also increases, but not necessarily in a linear fashion. As can be seen in the sub-figures, it is evident that the lowest inlet air velocities are obtained with 150 mm resulting in the lowest loss also the flow of the air is smooth and orderly.

The flow regime within the receiver is crucial. When velocities are low, the flow tends to be smooth and orderly, leading to a laminar pattern. However, at higher velocities, it can shift into irregular patterns, as demonstrated for the 200 mm receiver depth. Beyond a receiver depth of 150 mm, there is an increase in the inlet air velocity, resulting in a higher pressure drop, and the flow adopts an irregular pattern, consequently leading to a decrease in efficiency and subsequently reducing the ARR.

Analysis of the Gradient of Mass Flow and Temperature along the Receiver. A clarification for the impact of both the mass flow gradient and the temperature gradient along the receiver surface will be made. These gradients will be incorporated into the receiver through two distinct approaches. In the initial scenario, there will be an increase to the main absorber, while in the subsequent case, an increase will be made to the aperture.

The examination of these gradients provides valuable insights into how variations in mass flow and temperature can influence the overall performance of the receiver system. By specifically targeting the main absorber and aperture, the aim to gain a comprehensive understanding of the interaction between these factors and their effects on the system's efficiency limits. This investigation is important in optimizing the design and operation of the receiver for enhanced performance. As the maximum efficiency has been obtained for a receiver depth of 150 mm, the following analyses will be based on this variation.

Mass Flow Gradient. The open cavity receiver is partitioned into five segments of uniform height. This division serves to implement the mass flow gradients for CFD simulations under different mass flow loads.

In the analysis of mass flow gradients, adjustments will be applied in two distinct orientations: one towards the main absorber and the other to the aperture as shown in Figure 7. Furthermore, the mass flow gradients will be introduced at three varying levels, specifically 25% and 50% respectively for full load (0.0700 kg/s), 75% load (0.0525 kg/s), and 50% (0.0350 kg/s) load.

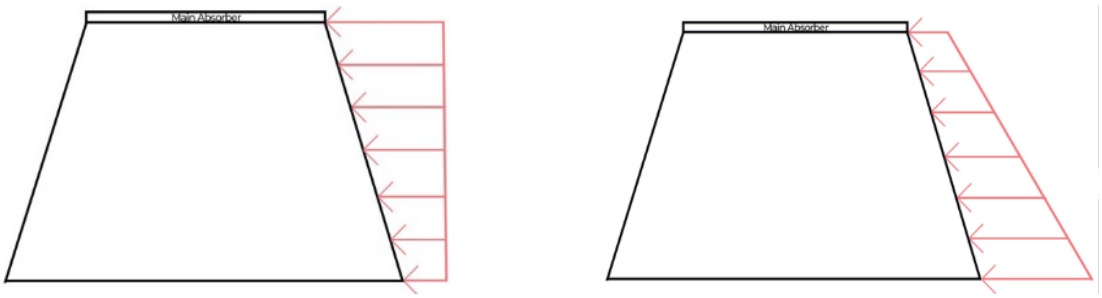

(a) Gradients Increasing to the main absorber (b) Gradients Increasing to the aperture

Figure 7. *Ilustration of the orientation of the relative mass flow gradients along the receiver*

To enhance comprehension, Figure 8 assigns numerical labels to the segments utilized for the introduction of the mass flow gradients. Corresponding values indicating the variation in mass flow for the mentioned scenarios are provided in Tables 3–8.

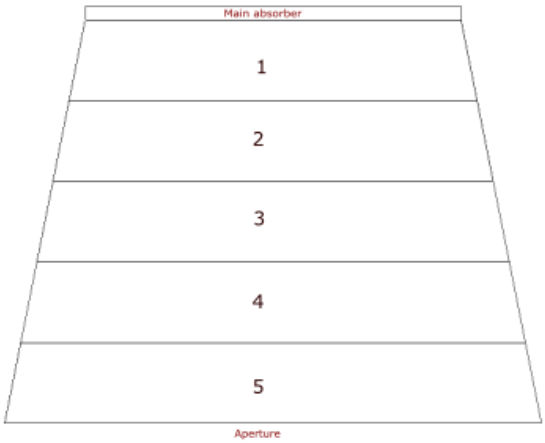

Figure 8. *Number labeling of the segments*

To illustrate the influence of the mass flow gradient, an observation centered around the utilization of a 150 mm receiver depth is presented, as it has demonstrated the highest ARR. The mass flow for each segment are calculated as shown in Equation (7) for different loads:

$$\dot{m}_{segment} = \frac{Area_{segment}}{Area_{total}} \cdot \dot{m}_{load} \tag{7}$$

Table 3. *Mass flow density distribution for full load*

Section	Uniform Mass Flow Density [kg/s·mm²]	50% gradient on Mass Flow Density to aperture [kg/s·mm²]	50% gradient on Mass Flow Density to the main absorber [kg/s·mm²]	25% gradient on Mass Flow Density to aperture [kg/s·mm²]	25% gradient on Mass Flow Density to the main absorber [kg/s·mm²]
1	6.729E-07	3.364E-07	9.053E-07	5.047E-07	7.912E-07
2	6.729E-07	5.047E-07	8.411E-07	6.056E-07	6.729E-07
3	6.729E-07	6.729E-07	6.729E-07	6.729E-07	6.729E-07
4	6.729E-07	8.411E-07	5.047E-07	6.729E-07	6.056E-07
5	6.729E-07	9.053E-07	3.364E-07	7.912E-07	5.047E-07

Table 4. *Mass flow distribution for full load*

Section	Uniform Mass Flow [kg/s]	50% gradient on Mass Flow to aperture [kg/s]	50% gradient on Mass Flow to the main absorber [kg/s]	25% gradient on Mass Flow to aperture [kg/s]	25% gradient on Mass Flow to the main absorber [kg/s]
1	0.0120	0.0060	0.0214	0.0090	0.0187
2	0.0130	0.0097	0.0187	0.0117	0.0164
3	0.0140	0.0140	0.0140	0.0140	0.0140
4	0.0149	0.0187	0.0097	0.0164	0.0117
5	0.0159	0.0214	0.0060	0.0187	0.0090
Total Mass Flow	0.0700	0.0700	0.0700	0.0700	0.0700

Table 5. *Mass flow density distribution for 75% load*

Section	Uniform Mass Flow Density [kg/s·mm²]	50% gradient on Mass Flow Density to aperture [kg/s·mm²]	50% gradient on Mass Flow Density to the main absorber [kg/s·mm²]	25% gradient on Mass Flow Density to aperture [kg/s·mm²]	25% gradient on Mass Flow Density to the main absorber [kg/s·mm²]
1	5.047E-07	2.523E-07	6.790E-07	3.785E-07	5.551E-07
2	5.047E-07	3.785E-07	6.308E-07	4.54E-07	5.551E-07
3	5.047E-07	5.047E-07	5.047E-07	5.047E-07	5.047E-07
4	5.047E-07	6.308E-07	3.785E-07	5.551E-07	4.542E-07
5	5.047E-07	6.790E-07	2.523E-07	5.551E-07	3.785E-07

Table 6. *Mass flow distribution for 75% load*

Section	Uniform Mass Flow [kg/s]	50% gradient on Mass Flow to aperture [kg/s]	50% gradient on Mass Flow to the main absorber [kg/s]	25% gradient on Mass Flow to aperture [kg/s]	25% gradient on Mass Flow to the main absorber [kg/s]
1	0.0090	0.0045	0.0161	0.0067	0.0140
2	0.0097	0.0077	0.0140	0.0087	0.0123
3	0.0105	0.0105	0.0105	0.0105	0.0105
4	0.0112	0.0140	0.0077	0.0123	0.0087
5	0.0119	0.0161	0.0045	0.0140	0.0067
Total Mass Flow	0.0525	0.0525	0.0525	0.0525	0.0525

Table 7. *Mass flow density distribution for 50% load*

Section	Uniform Mass Flow Density [kg/s·mm²]	50% gradient on Mass Flow Density to aperture [kg/s·mm²]	50% gradient on Mass Flow Density to the main absorber [kg/s·mm²]	25% gradient on Mass Flow Density to aperture [kg/s·mm²]	25% gradient on Mass Flow Density to the main absorber [kg/s·mm²]
1	3.364E-07	1.682E-07	4.526E-07	2.523E-07	3.956E-07
2	3.364E-07	2.523E-07	4.205E-07	3.028E-07	3.701E-07
3	3.364E-07	3.364E-07	3.364E-07	3.364E-07	3.364E-07
4	3.364E-07	4.205E-07	2.523E-07	3.701E-07	3.028E-07
5	3.364E-07	4.526E-07	1.682E-07	3.956E-07	2.523E-07

Table 8. *Mass flow distribution for 50% load*

Section	Uniform Mass Flow [kg/s]	50% gradient on Mass Flow to aperture [kg/s]	50% gradient on Mass Flow to the main absorber [kg/s]	25% gradient on Mass Flow to aperture [kg/s]	25% gradient on Mass Flow to the main absorber [kg/s]
1	0.0060	0.0030	0.0107	0.0045	0.0093
2	0.0065	0.0048	0.0093	0.0058	0.0082
3	0.0070	0.0070	0.0070	0.0070	0.0070
4	0.0074	0.0093	0.0048	0.0082	0.0058
5	0.0079	0.0107	0.0030	0.0093	0.0045
Total Mass Flow	0.0350	0.0350	0.0350	0.0350	0.0350

The variation of the ARR with regards to the mass flow gradient, whether introduced to the main absorber (see positive values) or applied inversely to the aperture (see negative values) is represented in Figure 9.

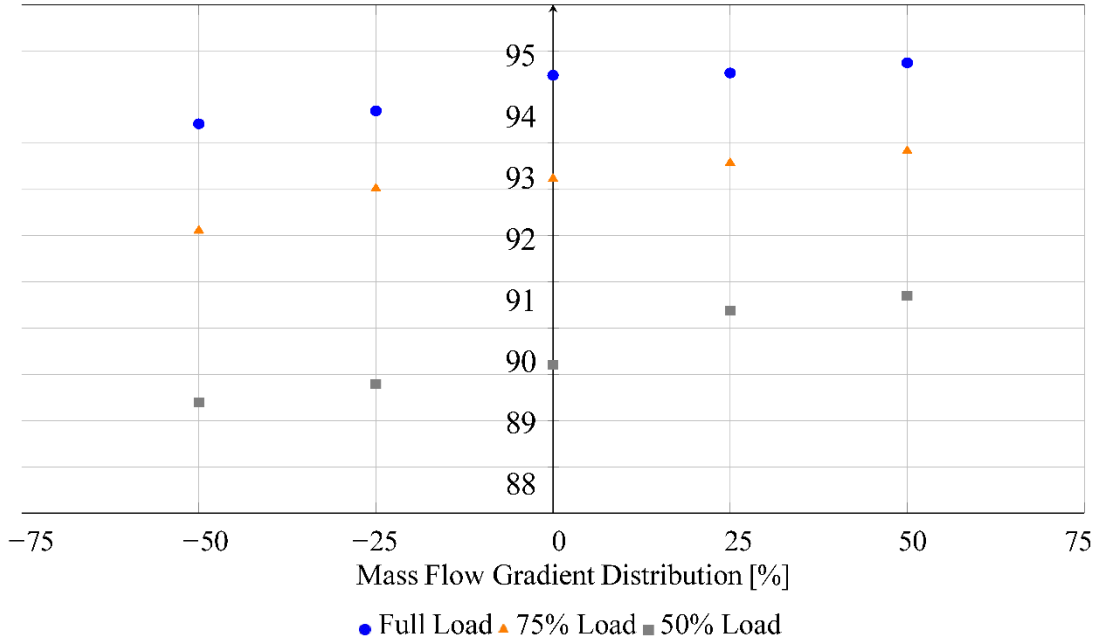

Figure 9. *ARR dependence on the mass flow gradient*

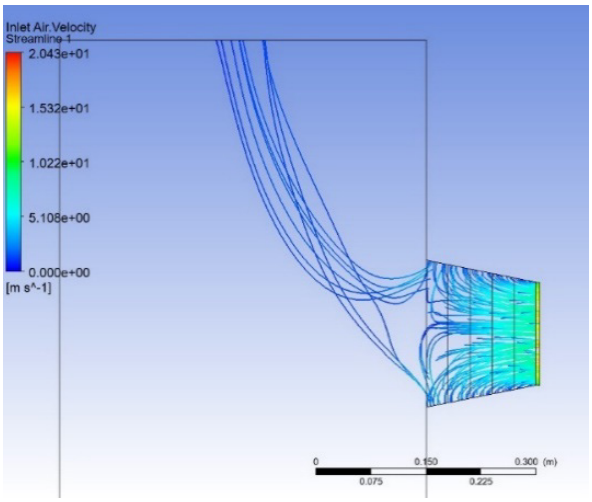

(a) Partial loss of warm air
for 50% mass flow gradient to the main absorber

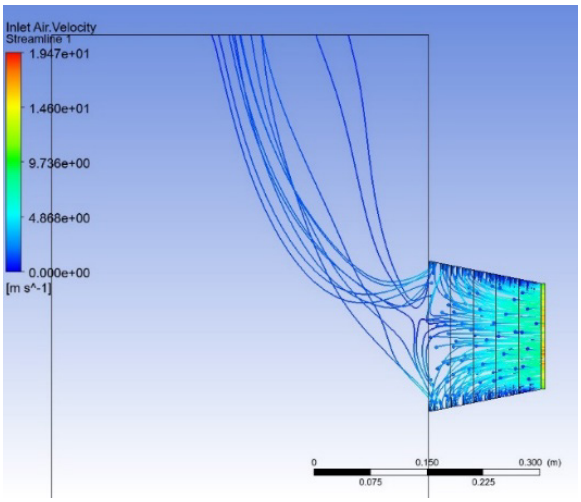

(b) Partial loss of warm air
for 50% mass flow gradient to aperture

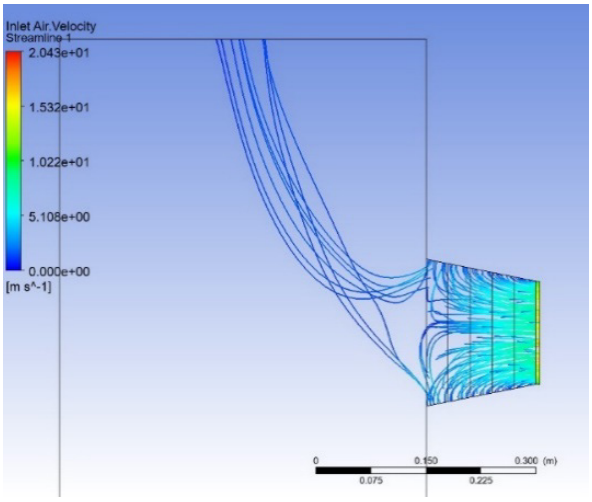

(c) Partial loss of warm air
for 25% mass flow gradient to the main absorber

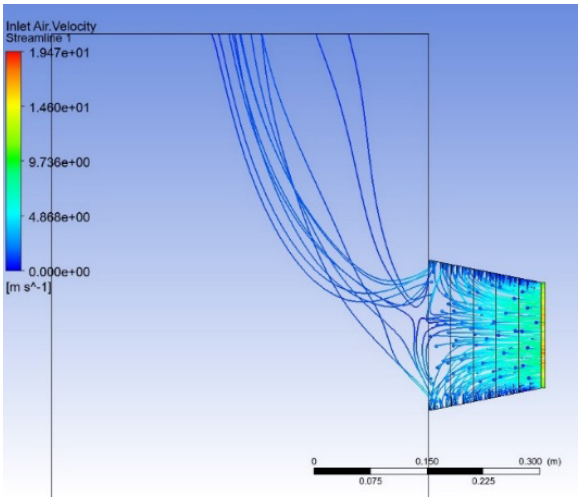

(d) Partial loss of warm air
for 25% mass flow gradient to aperture

Figure 10. *Comparison of the partial loss of warm air to the ambient for different geometry variations*

Increasing the overall mass flow typically results in an increase of the ARR. Nevertheless, it also brings about reduced air temperatures, consequently leading to distinct operational states for the receiver. Hence, the ARR changes in the depicted cases will be evaluated under the same load variations. While this implies that fine-tuning the mass flow is important for increasing system efficiency, it indicates a direct connection between the orientation of the applied mass flow density along the inlet of the receiver. This underscores the significance of the system design for enhanced performance an examination of the cavity's internal dynamics is imperative. Given the relatively consistent inlet air velocities, the examination of warm air loss to the surroundings becomes important for meaningful comparisons (Fig. 10).

Introducing higher mass flow gradients near to the aperture results in increased warm air losses to the environment, consequently increasing overall losses. Specifically, for a mass flow gradient distribution of 50%, the ARR experiences a reduction of roughly 1.5%, while for a distribution of 25%, it decreases by about 0.85%. This underscores the proportional decrease in ARR with increased mass flow near the aperture, as losses become more evident.

Temperature Gradient. Once more, the same method is applied that is used in the mass flow gradient approach, this time with the integration of the temperature gradients in both directions along the receiver. The utilized temperature gradients are set to be respectively 25°C, 50°C, and 75°C along the receiver for this analysis.

Figure 11 shows the ARR values obtained for different loads. It can be seen that incorporating a temperature gradient, by keeping the inlet mass flow constant, has almost no effect on the ARR distribution for the same load distributions.

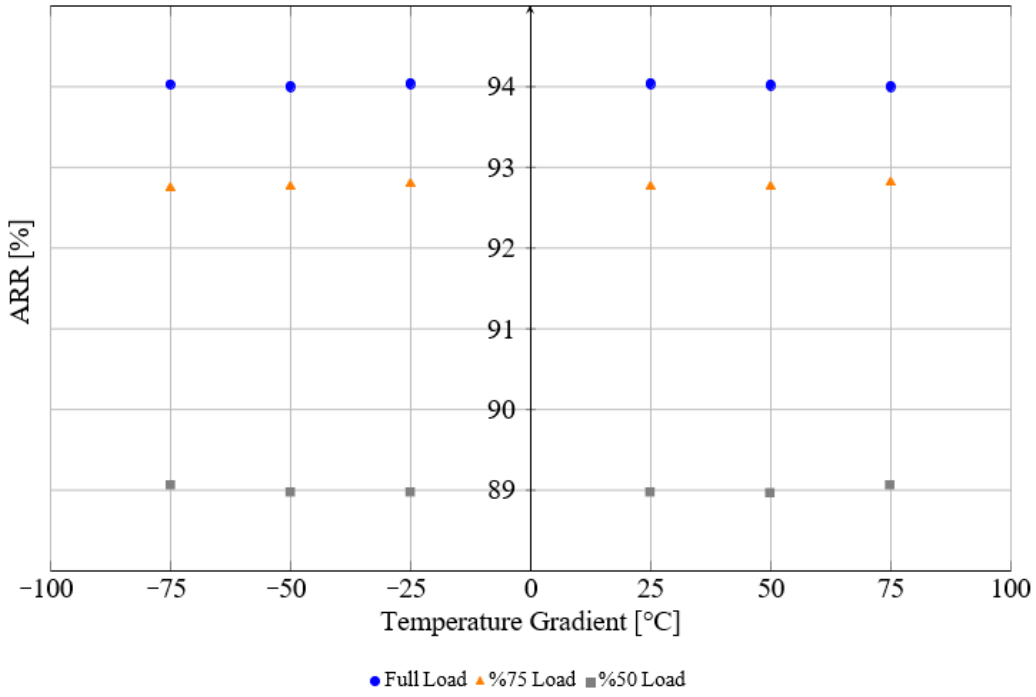

Figure 11. *ARR dependence on the temperature gradient*

The study delves into a comprehensive examination of the interior of the cavity receiver to gain a better understanding. This will involve investigations of both the temperature gradient and the assessment of the losses of the warm air to the ambient.

Furthermore, it is worth noting that the constant dissipation of heat to the ambient is a favorable outcome, as it signifies a stable thermal performance regardless of the applied temperature gradient. The results (Figures 12 and 13) indicate that the implemented temperature gradient influences the temperature distribution in proximity to the walls, but exerts minimal influence on the internal regions of the receiver. Consequently, this has a limited impact on the overall buoyancy forces and overall losses to the environment. Moreover, the heat dissipated to the surroundings remains nearly constant across all scenarios.

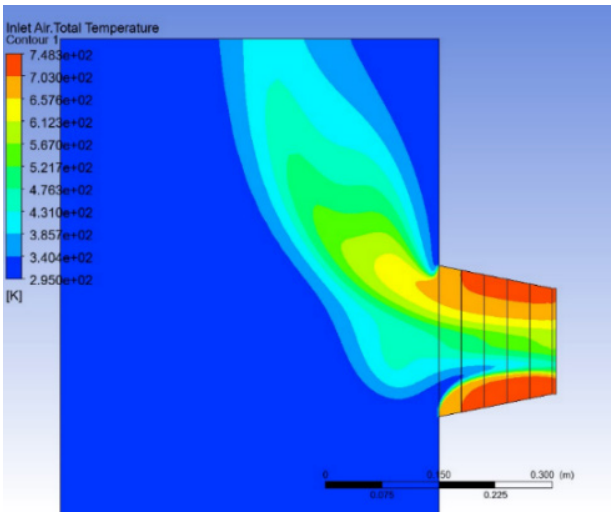

(a) Inlet air total temperature contour
for 25°C temperature gradient to the main absorber

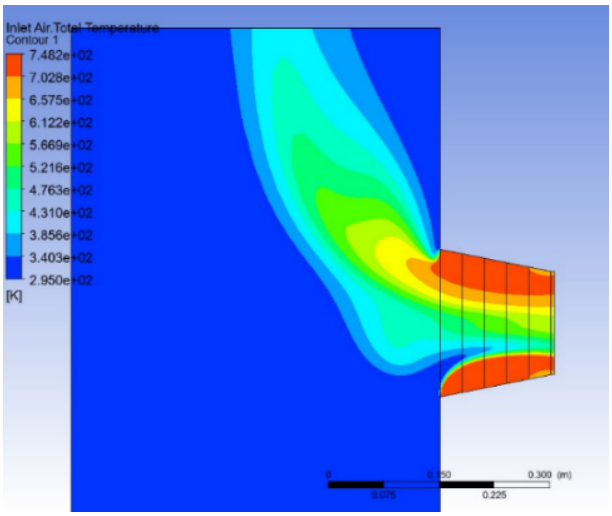

(b) Inlet air total temperature contour
for 25°C temperature gradient to aperture

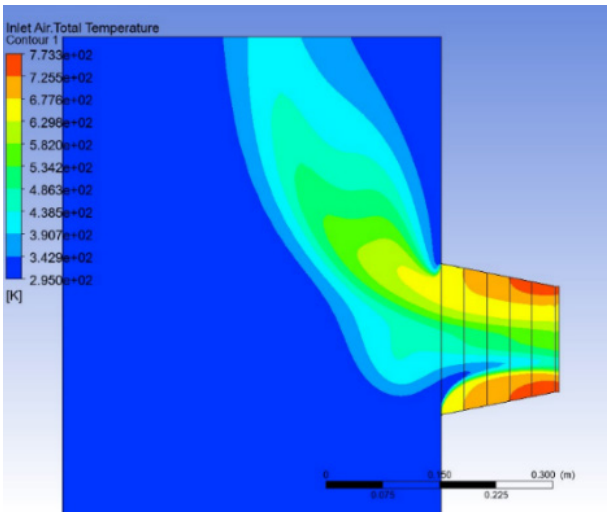

(c) Inlet air total temperature contour
for 50°C temperature gradient to the main absorber

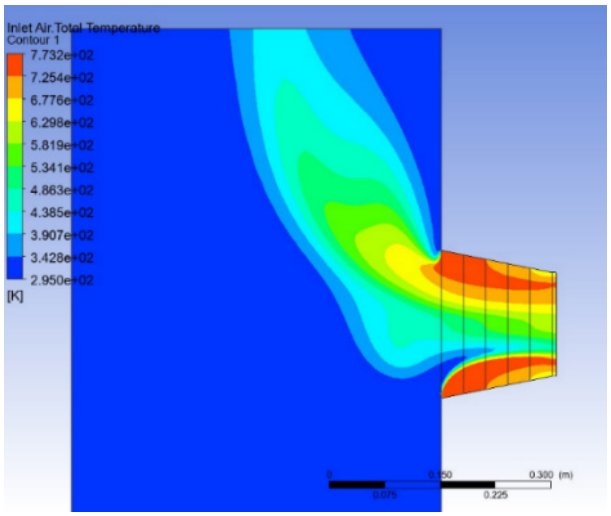

(d) Inlet air total temperature contour
for 50°C temperature gradient to aperture

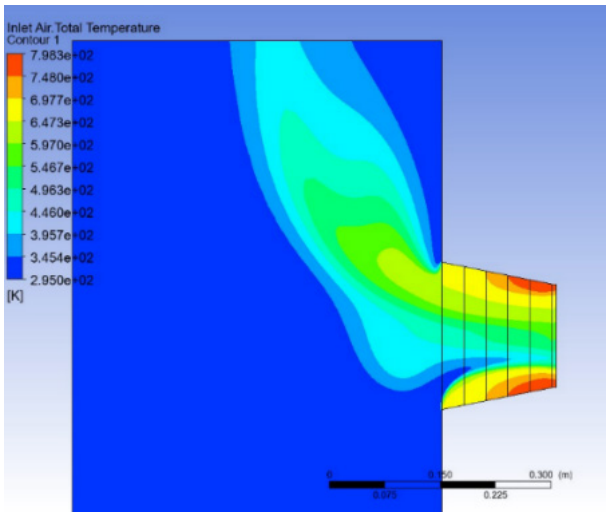

(e) Inlet air total temperature contour
for 75°C temperature gradient to the main absorber

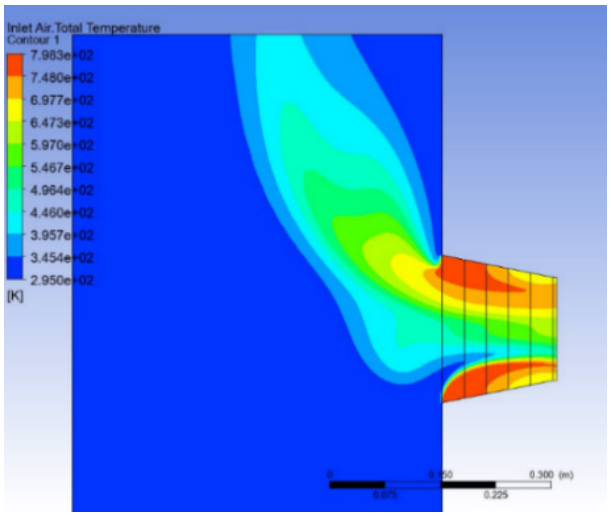

(f) Inlet air total temperature contour
for 75°C temperature gradient to aperture

Figure 12. *Comparison of the inlet air total temperature contour plots for different temperature gradients*

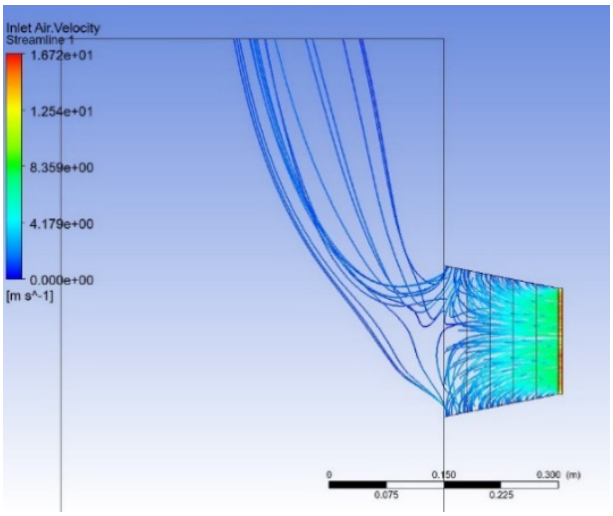

(a) Inlet air velocity contour
for 25°C temperature gradient to the main absorber

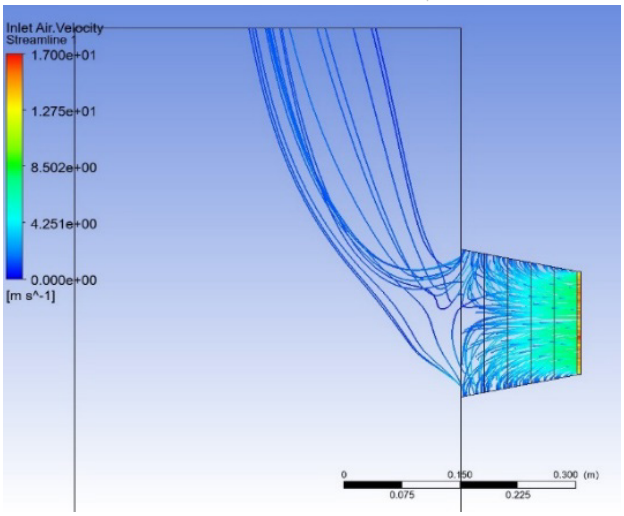

(b) Inlet air velocity contour
for 25°C temperature gradient to aperture

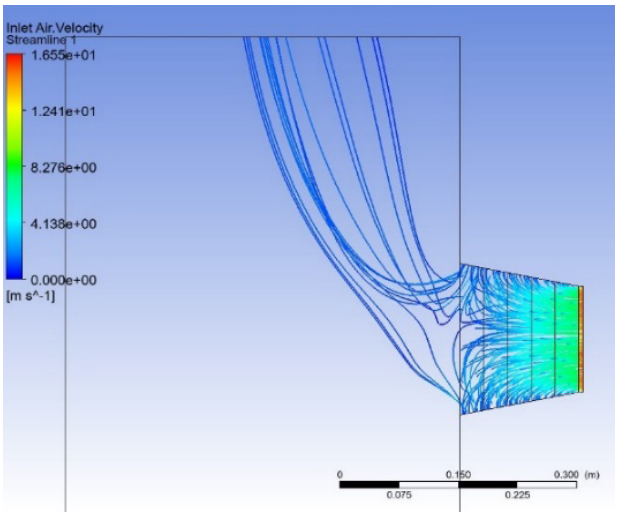

(c) Inlet air velocity contour
for 50°C temperature gradient to the main absorber

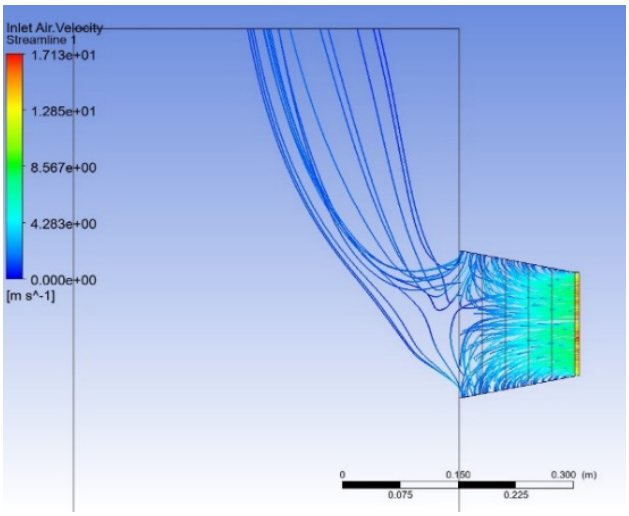

(d) Inlet air velocity contour
for 50°C temperature gradient to aperture

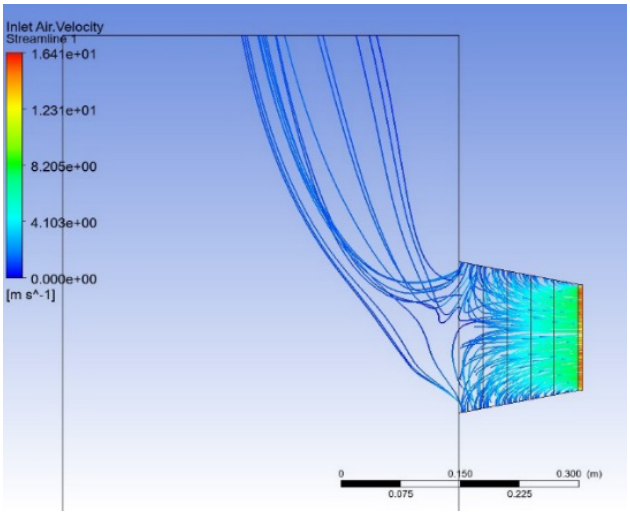

(e) Inlet air velocity contour
for 75°C temperature gradient to the main absorber

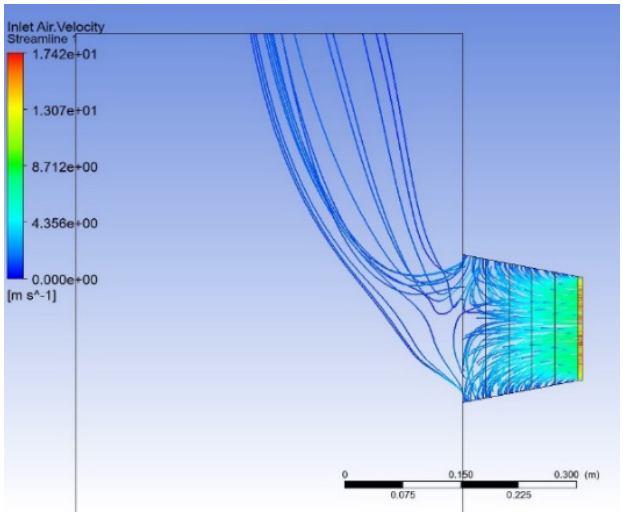

(f) Inlet air velocity contour
for 75°C temperature gradient to aperture

Figure 13. *Comparison of the inlet air velocity contour plots for different temperature gradients*

As previously discussed, in the scenarios illustrated above, the losses to the surroundings exhibit a nearly identical behavior. As a result, it does not affect the ARR in the same manner as changes in geometry or the implementation of mass flow gradients.

Conclusion

The study investigated two distinct approaches. The first approach was developed to find an optimal geometric variation for the receiver in terms of efficiency and subsequently, the aim of the second approach has been to analyze the influence of both mass flow and temperature gradients on it.

The models were generated and assessed within ANSYS environment. Given the relatively straightforward geometry, a structured mesh was employed, aligning well with such configurations. The *k*-omega-SST turbulence model was selected as the most fitting option, given the complexity of the flows being dealt with, as well as its advantageous near-wall treatment capabilities.

ARR represents the fraction of air redirected back into the system after being expelled or discharged. Investigations have showed that the ARR of the receiver is proportional with the efficiency of the receiver since a larger proportion of warm air is effectively reused.

Various analyses have been conducted to enhance the efficiency of the receiver. The model has shown that the pivotal factor in increasing ARR primarily depends on the depth of the receiver aperture. A transition from 50 mm to 150 mm in depth leads to an increase in ARR by 7.83%, and afterwards it shows a decrease of 0.3% as the depth reaches to 200 mm.

Furthermore, assessments of receiver performance encompassed the examination of the rate of change of air inlet mass flow and the response to a rate of change in temperature along the walls of the receiver. These analyses were conducted in both directions, focusing on both the main absorber and the receiver aperture. The comparative examination of the mass flow gradient reveals that increasing the load condition results in a higher ARR, exerting a more substantial impact compared to the orientation of the applied mass flow gradient. However, altering the loads brings about distinct operational states for the receiver since it leads to different air temperatures. As a result, conclusions will be drawn based on constant load variations.

The direction in which the mass flow gradient is applied becomes notably more influential as the proportion of the gradient is increased. For instance, with a 50% mass flow gradient, an ARR enhancement of 1.4% can be achieved when a higher gradient is applied in proximity to the main absorber. This underscores the significance of properly managing mass flow within the receiver system.

Analyses of temperature gradients indicate that introducing such gradients has lower impact on the distribution of ARR under equivalent loads. The applied temperature gradient does affect the flow distribution near the inlet walls but its influence on the internal regions of the receiver is minimal. As a result, it has limited effect on the convective heat losses because it effects on the buoyancy forces and the ARR remain limited.

Upon gathering the collected results, it becomes evident that an observation regarding the ideal configuration of the receiver and the gradients to be employed can be formulated. The receiver attains its highest ARR at full load when possessing a depth of 150 mm. By incorporating a mass flow gradient into the receiver, efficiency can be further elevated by up to 0.21% when the gradient is progressively applied closer to the main absorber. Notably, at this stage, applying a temperature gradient did not exhibit any noticeable influence on the ARR.

Declaration of competing interest

The authors declare that they have no known competing financial interests or personal relationships that could have appeared to influence the work reported in this paper.

References

[1] Khan, I.M., Asfand, F., Al-Ghamdi, S.G. (2023). *Progress in research and technological advancements of commercial concentrated solar thermal power plants.* Solar Energy. doi.org/10.1016/j.solener.2022.10.041.

[2] Pitz-Paal, R. (2020). *19 – Concentrating Solar Power.* Future Energy (Third Edition). doi.org/10.1016/B978-0-08-102886-5.00019-0.

[3] Stadler, H., Maldonado, D., Offergeld, M., Schwarzbözl, P., Trautner, J. (2019). *CFD model for the performance estimation of open volumetric receivers and comparison with experimental data*. Solar Energy. doi.org/10.1016/j.solener.2018.11.068.

[4] Romero M., Steinfeld, A. (2012). *Concentrating solar thermal power and thermochemical fuels*. Energy & Environmental Science. doi.org/10.1039/c2ee21275g.

[5] Zhang, W., Xie, P., Li, Y., Teng, L., Zhu, J. (2022). *3D CFD simulation of the liquid flow in a rotating packed bed with structured wire mesh packing*. Chemical Engineering Journal. doi.org/10.1016/j.cej.2021.130874.

[6] Cagnoli, M., Froio, A., Savoldi, L., Zanino, R. (2019). *Multi-scale modular analysis of open volumetric receivers for central tower CSP systems*. Solar Energy, 190, 195–211. doi.org/10.1016/j.solener.2019.07.076.

[7] Xijie, S., Yongyao, L., Liu, C., Zhengwei, W., Yan, J. (2023). *Numerical simulation and experimental study on an innovative vortex eliminator using a modified SST turbulence model for gas-liquid two-phase flow*. Ocean Engineering. doi.org/10.1016/j.oceaneng.2022.113383.

[8] Cheilyko, A., Göhring, F., Wieghardt, K. (2022). *Receiver efficiency as a determining criterion for the effectiveness of a solar tower*. International Conference on Science, Technology and Management (ICSTM – 2022), 23-24 Nov 2022, Paris, France.

[9] Springer VDI Heat Atlas. (2010). *B1 Fundamentals of Heat Transfer*. In: VDI Heat Atlas. doi.org/10.1007/978-3-540-77877-6.

[10] Cheilytko, A.O. (2014). *Use of secondary energy resources: a study guide for students of ZGIA, specialty 6.050601.* Heat and Power Engineering, full-time and part-time. Zaporizhzhia: ZGIA, 2014. 246 p.

[11] Rodriguez, J.I., Mills, A.F. (1996). *Heat transfer and flow friction characteristics of perforated-plate heat exchangers*. Experimental Heat Transfer. doi.org/10.1080/08916159608946529.

Acknowledgements

The authors would like to thank Kai Wieghardt of DLR for making this research possible, as well as for his support and inspiration.